

Decoupling and Coupling of the Host–Dopant Interaction by Manipulating Dopant Movement in Core/Shell Quantum Dots

Elan Hofman, Alex Khammag, Joshua T. Wright, Zhi-Jun Li, Peter Francis McLaughlin, Andrew Hunter Davis, John Mark Franck, Arindam Chakraborty,* Robert W. Meulenberg,* and Weiwei Zheng*



Cite This: *J. Phys. Chem. Lett.* 2020, 11, 5992–5999



Read Online

ACCESS |



Metrics & More

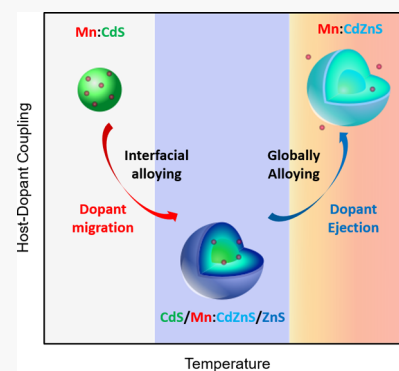


Article Recommendations



Supporting Information

ABSTRACT: Doping through the incorporation of transition metal ions allows for the emergence of new optical, electrical, and magnetic properties in quantum dots (QDs). While dopants can be introduced into QDs through many synthetic methods, the control of dopant location and host–dopant (H–D) coupling through directional dopant movement is still largely unexplored. In this work, we have studied dopant behaviors in Mn:CdS/ZnS core/shell QDs and found that dopant transport behavior is very sensitive to the temperature and microenvironments within the QDs. The migration of Mn toward the alloyed interface of the core/shell QDs, below a temperature boundary (T_b) at ~ 200 °C, weakens the H–D interactions. At temperatures higher than the T_b , however, dopant ejection and global alloying of CdS/ZnS QDs can occur, leading to stronger H–D coupling. The behavior of incorporated dopants inside QDs is fundamentally important for understanding doping mechanisms and the host–dopant interaction-dependent properties of doped nanomaterials.



Incorporation of transition metal ions as dopants into semiconductor quantum dots (QDs) can introduce new optical, electronic, and magnetic properties,^{1–11} making the doped QDs valuable components for applications in light-emitting devices, bioimaging, solar cells, and spintronics.^{12–16} The dopant sites (i.e., surface, core, or specific depth from the surface) inside the QDs determine the host–dopant (H–D) coupling from the overlap between the dopant and exciton wave functions of the host lattice.⁵ Therefore, the properties of doped QDs are strongly influenced by the dopant sites and/or location as demonstrated in Mn-doped CdS/ZnS core/shell QDs^{17–21} as well as Ag/Mn co-doped CdS/ZnS core/shell QDs²² with the Mn dopants grown at a specific surface layer during synthesis. Tuning the H–D coupling by controlling the dopant sites after incorporation into the host lattice, however, is challenging.

In the past two decades, many synthetic methodologies have been developed for introducing dopants inside QDs. Successful doping by dopant incorporation up to its solubility limit can be achieved by a predoped single-source precursor,^{7,8,23} nucleation doping,^{24,25} growth doping,^{17,26–28} and ion exchange and diffusion.^{3,29–31} Despite significant developments in the synthesis of doped QDs, there has been limited study of the mass transport behaviors of dopants as well as the change in the microenvironment of the host lattice after incorporation of the dopant inside QDs,^{32–34} or toward a mechanistic understanding of dopant behavior in the host core/shell lattice.

Recently, we found that the local composition of the host core/shell lattice, specifically at the core/shell interface, has a profound effect on the behavior of incorporated dopants inside the core/shell nanocrystals. We presented evidence that Mn(II) dopants migrate toward the alloyed interface of CdS/ZnS core/shell QDs¹⁹ and ZnSe/CdS/ZnS core/multi-shell nanowires³⁵ during shell passivation using the successive ion layer adsorption and reaction (SILAR) method. This directional dopant diffusion (i.e., dopant migration) can be initiated by the availability of dopant sites with smaller cationic size mismatch at the cation-alloyed interface of the core/shell nanocrystals and lead to weakened H–D interaction and decreased energy transfer efficiency. However, how to strengthen the H–D coupling by controlled dopant movements inside the QD lattice is unknown. Furthermore, it is still unclear if the outward dopant migration is a process similar to dopant ejection initiated during the self-purification process, which causes the removal of dopant ions from the host lattice during high-temperature annealing.^{33,34}

In this work, we have studied the mass transport of both dopants and the host lattice in Mn:CdS/ZnS core/shell QDs.

Received: June 15, 2020

Accepted: July 7, 2020

Published: July 7, 2020

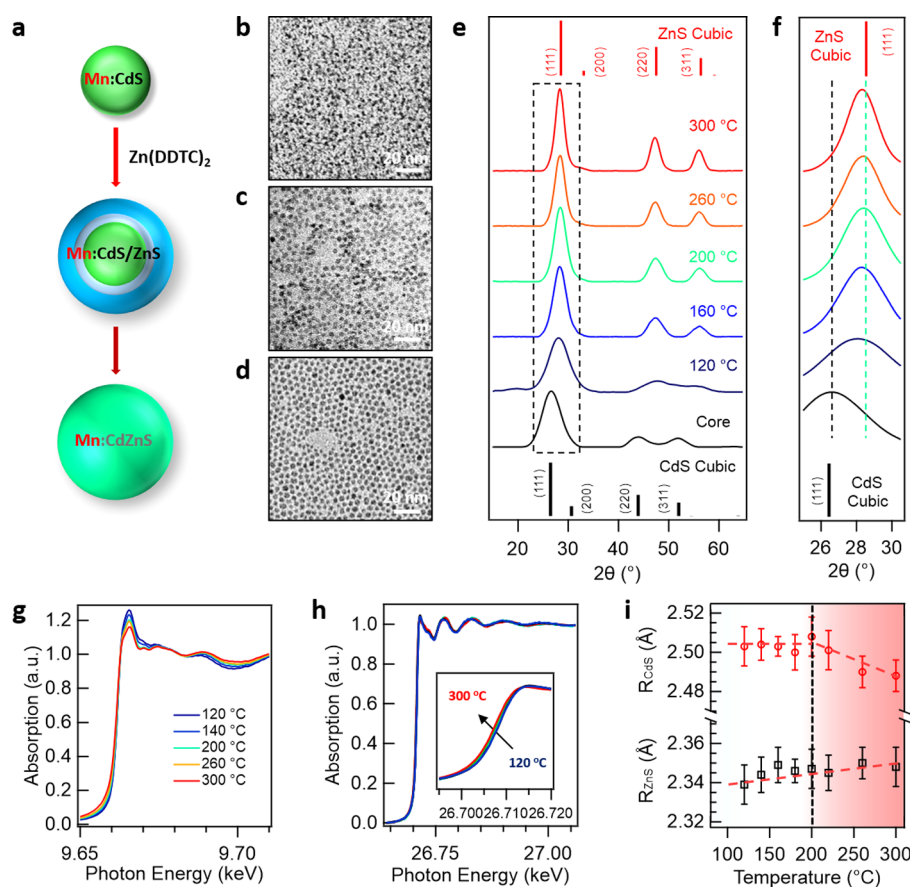


Figure 1. Size, structure, and microcomposition of Mn:CdS/ZnS core/shell QDs. (a) Schematic illustration of the variation of the composition of Mn:CdS/ZnS QDs during ZnS shell passivation. (b–d) Transmission electron microscopy images of Mn:CdS core and selective Mn:CdS/ZnS core/shell (200 and 300 °C) QDs. (e) Powder XRD patterns of Mn:CdS core and selective Mn:CdS/ZnS core/shell QDs (120, 160, 200, 260, and 300 °C). (f) Close-up of XRD patterns of the (111) diffraction peak. (g) Zn K-edge XANES and (h) Cd K-edge XANES for Mn:CdS/ZnS QDs as a function of temperature. (i) Cd–S and Zn–S bond lengths as obtained from EXAFS fits vs temperature.

Three distinct stages with different H–D couplings are observed during the ZnS shelling process, including (I) surface dopant replacement during the initial ZnS passivation, (II) migration of the dopant toward the alloyed interface of CdS/ZnS core/shell QDs, and (III) global alloying of host QDs and dopant ejection above a temperature boundary (T_b , ~ 200 °C).

Mn:CdS QDs of 3.0 nm average size (Figure 1b) were synthesized through a colloidal hot-injection method.¹⁹ We prepared Mn:CdS/ZnS core/shell QDs utilizing a highly reactive zinc- and sulfur-containing precursor, zinc diethyldithiocarbamate [$\text{Zn}(\text{DDTC})_2$],³⁶ for ZnS shell growth (Figure 1a and the Supporting Information). This single-source shelling precursor (SSSP) method allows us to monitor the mass transport of both host cations and dopants over a wider temperature range (120–300 °C in this study) compared with that of the typical SILAR method for shell coating. The size of the core/shell QDs increases gradually, with the diameters of the core/shell QDs being 3.8 ± 0.3 , 4.6 ± 0.3 , 5.1 ± 0.4 , and 5.5 ± 0.5 nm at 120, 160, 200, and 260 °C, respectively (Figure 1c,d and Figures S1 and S2). The size of the core/shell QDs remains constant for the following reaction period (260–300 °C). During ZnS shell growth, the X-ray diffraction (XRD) peaks experience a systematic shift to larger angles toward zinc blend phase ZnS until 200 °C, followed by a small shift to smaller angles with an increase in temperature (Figure 1e,f and Figure S3). The shift of the diffraction peaks to smaller angles indicates the formation of globally alloyed QDs

($\text{Cd}_{1-x}\text{Zn}_x\text{S}$) with intermediate lattice parameters (Table S1), as the result of high-temperature annealing (>200 °C). Using the peak position of the (111) diffraction peak of the core and core/shell QDs, the $d_{(111)}$ spacing and the average metal–sulfur (M–S) bond length were calculated (Figure S3 and Table S1). Analyzing the M–S bond length, we found an initial length of 2.503 Å for the Mn:CdS core QDs followed by a continuous drop upon shelling until the reaction mixture reached 200 °C (2.353 Å), which is caused by the addition of ZnS with a lattice parameter ($a = 5.41$ Å) that is smaller than that of CdS ($a = 5.82$ Å) atop the Mn:CdS core. Once the T_b had been crossed, a slight increase in the average bond length occurred due to the global alloying, resulting in a final bond length of 2.362 Å. It should be noted that the final bond length is much closer to the standard Zn–S bond length rather than an intermediate X–S bond length from globally alloyed Mn: $\text{Cd}_{1-x}\text{Zn}_x\text{S}$ QDs, which might indicate a ZnS-rich surface of the alloyed QDs.

To further probe the temperature-dependent composition variation within the core/shell QDs, X-ray absorption fine structure (XAFS) measurements were conducted to study the atomic bonding parameters of the QDs. The intensity of the Zn K-edge X-ray absorption near-edge structure (XANES) consistently decreases as a function of temperature (Figure 1g and Figure S4 and Table S2), suggesting substitution of a larger Cd atom into the ZnS lattice, which is consistent with Zn K-edge XANES simulations (Figure S5). The fitting of the

extended XAFS (EXAFS) data (Figure S4) shows an immediate increase in Zn–S bond length during shell passivation (Figure 1i), which is consistent with the incorporation of surface Cd cations from the CdS core into the ZnS lattice, as expected for the formation of the alloyed surface/interface ($T < T_b$; ~ 200 °C) and alloyed QDs ($T > T_b$) (Figure 2a, inset). The Cd–S bond length, however, from

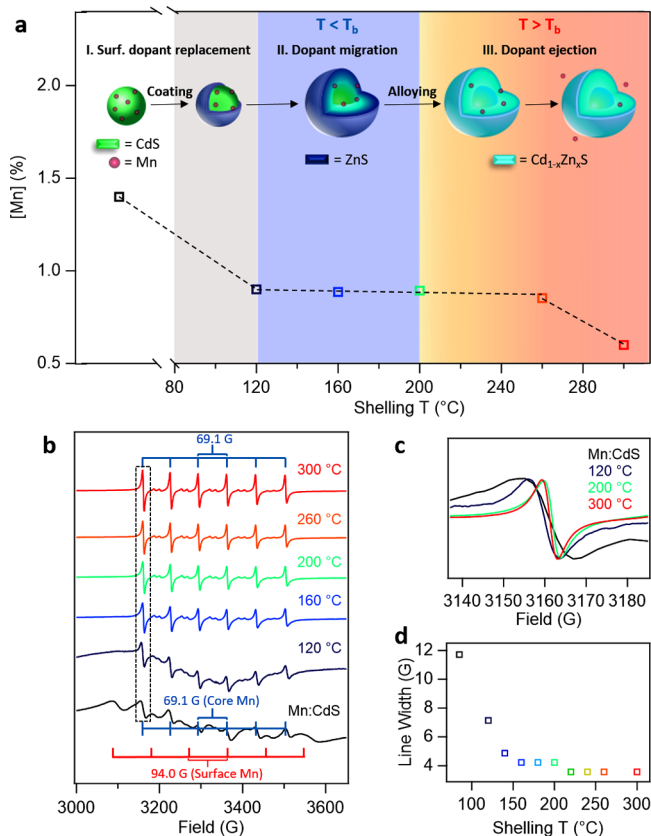


Figure 2. Three different dopant behaviors with different doping environments during ZnS shell passivation at different temperatures. (a) Mn doping concentration in Mn:CdS core and Mn:CdS/ZnS core/shell QDs throughout the shelling process. The inset shows temperature-dependent dopant replacement (stage I), migration (stage II), and ejection (stage III) during ZnS shell passivation. (b) Room-temperature X-band EPR spectra of Mn:CdS core and Mn:CdS/ZnS core/shell QDs (a). Two discrete sites for the Mn(II) occupying a substitutional Cd(II) site within the core ($A_{\text{core}} = 69.1$ G) and surface ($A_{\text{surface}} = 94.0$ G) are labeled for the Mn:CdS QDs. Only the Mn core site ($A_{\text{core}} = 69.1$ G) is observed for Mn:CdS/ZnS core/shell QDs grown above 120 °C. (c) Close-up view of the first peak of the Mn core EPR signal from panel b. (d) Linewidth of the first peak of the core Mn EPR signal during ZnS shell passivation.

the Cd K-edge EXAFS fitting (Figure S6 and Table S2) does not initially change and exhibits a significant shift of only the Cd K-edge XANES onset (Figure 1h) above T_b . This is due to the CdS core being largely undisturbed with only a small fraction of the surface Cd actually alloying with Zn to form the alloyed interface below T_b . Above T_b , the Cd K-edge XANES shifts to a lower energy (~ 1 eV) and the Cd–S bond length gradually decreases, which is consistent with a complete alloy transformation as suggested via XRD (Figure 1f,h and Table S1).

Inductively coupled plasma optical emission spectrometry (ICP-OES) measurements indicate a 1.4% Mn doping

concentration [calculated as the $\text{Mn}/(\text{Cd} + \text{Mn})$ ratio (Table S3)] for Mn:CdS QDs (Figure 2a). The Mn(II) ions exhibit a Poisson distribution within the QD ensemble, but on average this represents ~ 7 Mn(II) ions distributed stochastically between the core and surface per 3.0 nm Mn:CdS QD. The Mn(II) concentration decreases to 0.9% [~ 5 Mn(II) ions per QD] after the growth of the ZnS shell at 120 °C (stage I, initial surface dopant replacement) and remains unchanged for core/shell QDs grown up to 260 °C, indicating partial surface dopant removal during the initial shell coating process.^{17,37} The Mn(II) concentration decreases to 0.6% [~ 3 Mn(II) ions per QD] for the core/shell QDs grown at 300 °C, indicating dopant ejection at high temperatures.

Two sets of electron paramagnetic resonance (EPR) hyperfine splitting patterns were observed in the Mn:CdS QDs with hyperfine constants (A) equaling 69.1 and 94.0 G (Figure 2b and Figure S7), which are attributed to Mn(II) located within the core lattice and on the QD surface, respectively.^{38,39} In addition, a broad dipolar background of the EPR indicates the presence of short-range Mn–Mn interactions in the CdS QDs.³⁵ During ZnS shell passivation, both the dipolar term and the surface hyperfine in EPR spectra are largely quenched, resulting in the presence of a single core hyperfine term at high temperatures (Figure 2b and Figure S7). A weaker dipolar contribution in EPR for the QDs grown at 120 °C can still be observed. However, the decreased dipolar contribution from 120 to 160 °C (and above) during ZnS shell passivation indicates larger Mn–Mn distances caused by dopant ion migration,³⁵ considering the same doping concentration in those QDs.

In addition, the linewidth of the Mn EPR hyperfine peak during ZnS shell passivation continually narrowed from 11.7 G for Mn:CdS QDs to 3.6 G for the doped globally alloyed CdZnS QDs grown at 300 °C (Figure 2c,d). The narrower EPR peak linewidth indicates weaker Mn–Mn interactions and less local strain on the Mn(II) dopant sites.^{19,40} For Mn incorporation inside CdS QDs, a large strain from the 13% cationic size mismatch between Cd(II) and Mn(II) ions can introduce an anisotropic distortion of the Mn ligand-coordinating environment, leading to a broad Mn EPR peak linewidth. However, considering the size of Mn(II) ions (80 pm) as being intermediate between those of Cd(II) (92 pm) and Zn(II) (74 pm),^{19,37,41} a smaller strain could be obtained from the Mn-doped CdZnS alloyed lattice compared with that of Mn:CdS QDs. Therefore, the alloyed lattice can more readily accommodate Mn ions,³⁷ and migration of Mn toward the CdZnS-alloyed interface (stage II) or globally CdZnS-alloyed QDs (stage III) leads to a smaller strain and a narrower Mn EPR peak (Figure 2b–d).

Figure 3a depicts the absorption and photoluminescence (PL) spectra of the QDs during ZnS shell passivation. The Mn:CdS QDs have a single emission peak centered at ~ 580 nm from the Mn(II) 4T_1 to 6A_1 transition (Figure 3a), implying strong coupling between the CdS host and Mn(II) dopants. When the sample reached 140 °C in stage I, a second PL peak emerges at 424 nm, which was identified as the CdS band-edge PL. Interestingly, as the reaction temperature increases, the PL ratio of the CdS and the Mn(II) increases from zero (at 120 °C) to a maximum value of 2.0 at T_b (~ 200 °C) (stage II), followed by a rapid decrease reaching 0.13 at 300 °C (stage III) (Figure 3b). The complete color change of stages I–III can be seen in the Commission International de l'Éclairage chromaticity coordinates (Figure 3c), as well as in

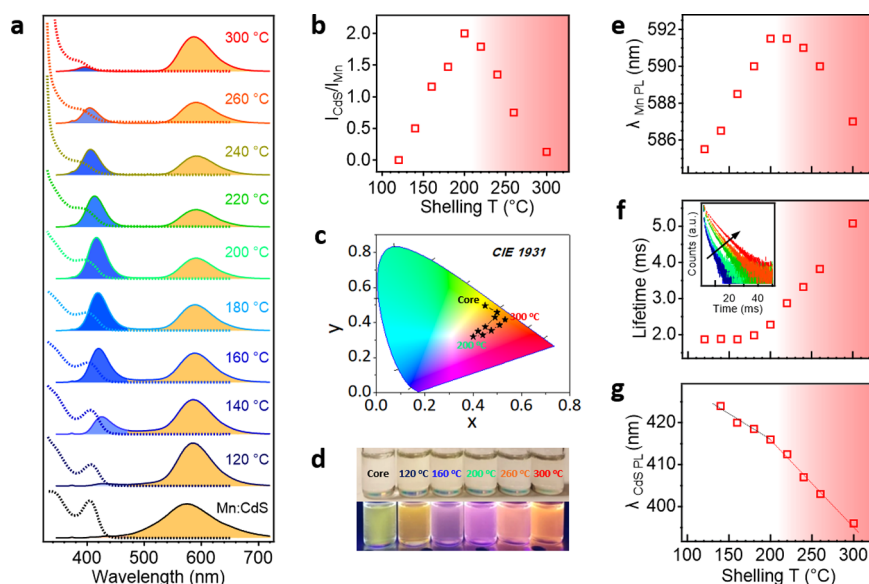


Figure 3. Optical properties of Mn:CdS core and Mn:CdS/ZnS core/shell QDs. (a) Normalized optical absorption (dotted lines) and emission (solid lines) of Mn:CdS QDs and Mn:CdS/ZnS core/shell QDs. (b) PL intensity ratio of CdS and Mn. (c) Commission International de l’Eclairage (CIE) chromaticity coordinates. (d) Optical images of the samples under room (top) and UV (bottom) light. (e) Central portion of the Mn(II) emission peak. (f) Derived Mn(II) PL lifetimes. (g) Center of the CdS PL peak of the Mn:CdS/ZnS QDs as a function of shelling temperature. The inset shows the Mn(II) PL decay kinetics as a function of shelling temperature.

the optical images of the samples under room and ultraviolet (UV) light (Figure 3d).

The rate of energy transfer between the exciton and Mn ions can be interpreted quantitatively using eq 1:⁴²

$$\frac{I_{\text{Mn}}}{I_{\text{BG}}} = n\Phi_{\text{Mn}} \frac{k_{\text{ET}} \lambda_{\text{BG}}}{k_{\text{UD-R}} \lambda_{\text{Mn}}} \quad (1)$$

where I_{Mn} and I_{BG} are intensities of the Mn emission and band gap PL of doped QDs, respectively, n is the number of Mn ions doped inside one QD, λ_{BG} is the wavelength of the exciton emission, λ_{Mn} is the wavelength of the Mn emission, Φ_{Mn} is the emission efficiency of a Mn ion, $k_{\text{UD-R}}$ is the radiative relaxation rate constant of an undoped QD, and k_{ET} is the rate constant for the transfer of energy from the exciton to a Mn dopant. Considering the small changes in the host and dopant PL position, as well as the same doping concentration below 260 °C, the host-to-dopant energy transfer rate k_{ET} is proportional to the PL ratio of Mn and the host lattice ($I_{\text{Mn}}/I_{\text{BG}}$).^{5,19,40} Because k_{ET} is related to the overlap between the wave functions of exciton and Mn dopants, the distance between exciton and Mn ions, the ratio of Mn(II) and QD emission could be used as an optical “gauge” to monitor H–D coupling and dopant sites inside the core/shell QDs. The increased CdS to Mn PL ratio from 120 to 200 °C (stage II, Figure 3a,b) indicates weakening of the host–dopant energy transfer (k_{ET}), which can be attributed to less wave function overlap between the host QDs and Mn dopants due to the outward migration of the dopant to the alloyed interface ($\text{Cd}_{1-x}\text{Zn}_x\text{S}$). Surprisingly, the PL ratio decreases at temperatures above 200 °C, indicating strengthened H–D coupling, which cannot be simply explained by migration of the dopant toward the interface or even the surface of the core/shell QDs. The strengthened H–D coupling at high temperatures can be understood, however, by the global alloying of the core/shell QDs at $T > T_b$, which leads to the largely delocalized exciton

throughout the alloyed QDs and the efficient overlap between the dopant and exciton wave functions.

It should be noted that the host–dopant energy transfer might compete with defect levels and nonradiative relaxation pathways within the QDs. To verify that the change in the PL ratio between the host QDs and Mn is dominated by H–D coupling rather than the changes of the surface traps during ZnS coating, we synthesized undoped CdS/ZnS core/shell QDs using the same shell coating procedure. It was found that the PL quantum yields (QYs) of undoped CdS/ZnS QDs are similar to the total PL QYs of Mn:CdS/ZnS QDs from host and Mn PL at the same reaction temperatures (Figure S8). Interestingly, slightly higher total PL QYs in Mn:CdS/ZnS QDs compared with that of undoped CdS/ZnS QDs at most of the temperatures were observed, which could be attributed to the fast H–D energy transfer that can efficiently compete with nonradiative relaxation pathways.^{40,43} However, the difference in PL QYs between the corresponding doped and undoped core/shell QDs is <10%. Therefore, it is reasonable to assume similar nonradiative relaxation rates for the corresponding doped and undoped QDs.^{19,35,40} On the basis of the assumption described above, the efficiency of H–D energy transfer (Φ_{ET}) can be estimated by a flowing equation using steady-state approximation:⁴⁰

$$\Phi_{\text{ET}} = 1 - \frac{\text{QY}_{\text{BG}}}{\text{QY}_{\text{UD}}} \approx \frac{\text{QY}_{\text{Mn}}}{\text{QY}_{\text{UD}}} \quad (2)$$

where QY_{BG} and QY_{Mn} are the band gap and Mn PL QY of doped QDs, respectively, and QY_{UD} is the band gap PL QY of the undoped QDs. It was found that Φ_{ET} for the Mn:CdS/ZnS QDs decreased from 1.86 to 0.50 when the shelling temperature increased from 120 to 200 °C followed by an increased Φ_{ET} at $T > T_b$ (1.02 at 300 °C) (Figure S9a). This result is consistent with the weakening and strengthening of the H–D decoupling below and above T_b , respectively. The smaller final Φ_{ET} of Mn:CdZnS-alloyed QDs at 300 °C (1.02)

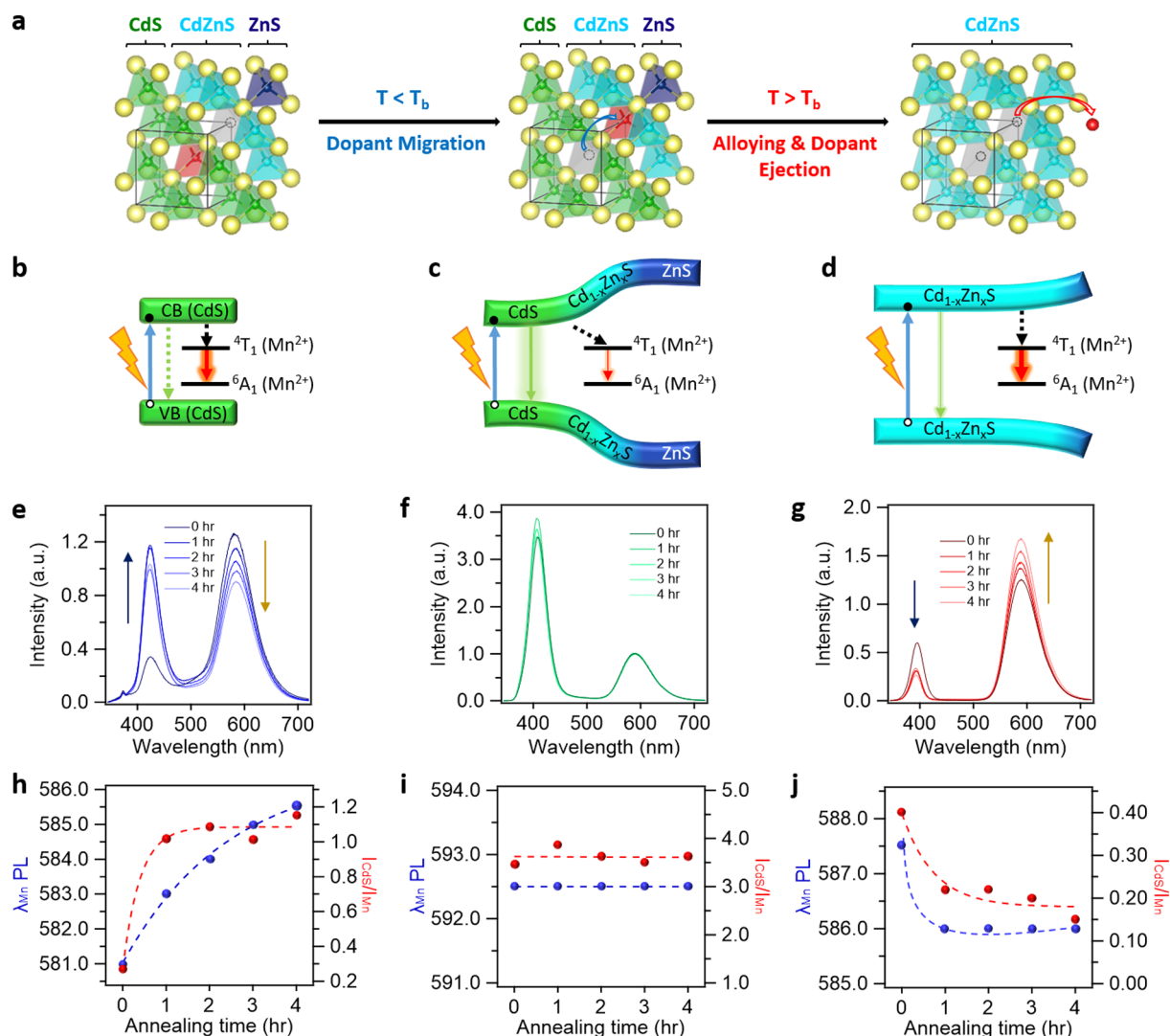


Figure 4. (a) Temperature-dependent dopant behavior and microenvironments of the host lattice within the CdS/ZnS cubic lattice. Green, light blue, dark blue, and red tetrahedra represent CdS, CdZnS, ZnS, and MnS units, respectively. Illustrations of (b) core Mn: CdS QD, (c) Mn: CdS/ZnS core/shell (below T_b) QD, and (d) Mn: CdS/ZnS core/shell (above T_b) QD energy levels and energy transfer diagrams (not to scale). PL, Mn PL peak position, and PL intensity ratio of CdS and Mn of Mn: CdS/ZnS core/shell QDs annealed at (e and h) 120 °C, (f and i) 200 °C, and (g and j) 300 °C from 0 to 4 h.

compared with that of Mn: CdS/ZnS QDs initially formed at 120 °C (1.86) might be due to lower Mn concentrations as a result of high-temperature dopant ejection as well as the near surface Mn doping in the alloyed QDs.

On the basis of the Φ_{ET} data, we further calculated the Mn emission efficiency (Φ_{Mn}) using eq 3.

$$\Phi_{Mn} = \frac{k_{Mn-R}}{k_{Mn-R} + k_{Mn-NR}} = \frac{QY_{Mn}}{\Phi_{ET}} \quad (3)$$

The radiative rate constant k_{Mn-R} is a function of the dipole matrix element between the ⁴T₁ and ⁶A₁ states of the Mn dopants.^{17,40} The nonradiative rate constant k_{Mn-NR} depends on the microenvironment of Mn dopants and its local modes.⁴⁰ Therefore, k_{Mn-NR} could change substantially with the location of Mn in the QDs. Because of the 13% size mismatch between Cd(II) and Mn(II) ions, the strain on Mn dopant sites inside CdS QDs can lead to a larger k_{Mn-NR} ^{19,37,40} than in the CdZnS-alloyed lattice. Indeed, the calculated Φ_{Mn} of the doped QDs using eq 3 increases dramatically during shell growth (Figure S9b), which can support the migration of Mn(II) to the

alloyed interface in stage II and further ejection through the globally alloyed QDs in stage III.

The temperature-dependent dopant behavior within the QDs can also be supported by the analysis of the Mn PL peak position (Figure 3e). Ithurria et al. have reported that the Mn PL can be used as a radial pressure gauge in core/shell QDs, and additional pressure arising from shell passivation can induce a Mn PL red-shift using a spherically symmetric elastic continuum model.⁴⁴ The large red-shift in the Mn(II) PL from 575 to 583 nm upon shelling at 120 °C indicates the rapid deposition of ZnS onto the Mn: CdS QDs. With an increasing ZnS shell thickness in stage II, the Mn(II) emission peak continues to red-shift until it reaches a maximum wavelength of 591.5 nm at 200 °C, which is consistent with the increasing pressure from thicker ZnS shells.⁴⁴ In stage III, however, a steady blue-shift of the Mn PL suggests decreased pressure from the ZnS shell applied on the Mn ions as a result of outward dopant ejection. The PL excitation (PLE) spectra (monitoring the Mn PL peak maximum) follow the same trend as absorption and PL spectra (Figure S10), further confirming

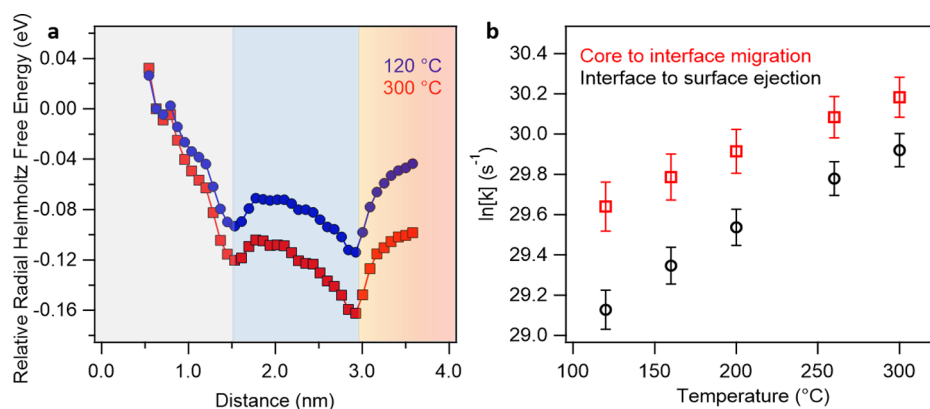


Figure 5. Density functional theory (DFT) calculation of dopant behavior. (a) Average relative free energy of the Mn(II) ion, quantum dot, and solvent system as the Mn(II) ion moves radially through CdS/ZnS at the lowest (120 °C) and highest (300 °C) temperature from the experimental study. (b) Rate constants of reactions for the Mn(II) ion in both CdS/ZnS and CdS host lattice systems as a function of temperature.

that the Mn PL originates from the transfer of energy from the host core/shell QDs (stage II) and alloyed QDs (stage III).

Time-resolved emission measurements show a slow increase in the Mn PL lifetime of Mn: CdS/ZnS core/shell QDs grown during stage II (Figure 3f), which is consistent with an increased Mn–Mn distance,³⁵ due to the relatively slow migration of the dopant toward the interface below T_b . However, a rapid increase in the Mn PL decay lifetime, from 2.3 to 5.0 ms (Figure 3f, Figure S11, and Table S4) for the QDs grown in stage III, indicates more isolated Mn centers from the reduction of the “concentration quenching” from short-range Mn–Mn interactions,^{45,46} which supports fast dopant ejection under high thermal energy in the alloyed QDs. The formation of the alloyed interface and alloyed QDs are further evidenced by the gradual blue-shift of the host lattice PL (~ 7 nm, -0.13 nm/°C) in stage II and a rapid shift (~ 20 nm, -0.20 nm/°C) in stage III (Figure 3g).

The culmination of our data suggests that dopant migration in the presence of the alloyed interface in core/shell QDs has an activation energy that is lower than that of dopant ejection and can occur at $T < T_b$ compared to dopant ejection due to self-purification ($T > T_b$) (Figure 4a). At $T < T_b$, the doped Mn ions can migrate toward a thin alloyed interface of the core/shell QDs, most likely mediated by cation vacancies,^{19,47} considering that half of the tetrahedral sites and all octahedral sites are empty in the cubic close packed S anions. Dopant migration leads to partial decoupling of CdS–Mn(II) interaction with a lower energy transfer efficiency; therefore, a new CdS PL can be observed in addition to Mn PL (Figure 4c). With sufficient thermal energy at $T > T_b$, global alloying of QDs can occur, accompanied by dopant ejection. The global alloying of the QDs results in a largely delocalized host exciton wave function and therefore strong H–D coupling with efficient energy transfer from host QDs to Mn dopants regardless of the location of the dopant inside the QDs (Figure 4d).

To further confirm the temperature-dependent dopant behaviors and H–D coupling, we thermally annealed the doped core/shell QDs grown below, at, and above T_b up to 4 h (Figure 4e–g and Figures S12 and S13). Below the T_b (120 and 160 °C), the continuous increase in the CdS:Mn PL ratio and weakened H–D coupling were observed due to the outward migration of the dopant to the alloyed interface (Figure 4e,h). The core/shell QDs annealed at the T_b (200 °C) exhibit a nearly constant CdS:Mn PL ratio and Mn PL

central peak position throughout the 4 h annealing (Figure 4f,i), which indicates the similar H–D coupling during the annealing process without further outward dopant movement. Once the core/shell QDs were annealed above the T_b [220, 240, and 300 °C (Figure 4g,j and Figures S12 and S13)] a slight blue-shift in Mn peak position was observed, which is consistent with dopant ejection leading to less overall pressure being applied to Mn ions. In addition, a decreased PL ratio with more prominent Mn PL confirms the continued delocalization of the host exciton throughout the QDs, activating the Mn PL relaxation pathway, due to global alloying.

The thermodynamics of the dopant migration and ejection was also investigated computationally by evaluating the relative effective radial Helmholtz free energy $\Delta A_{\text{eff}}(r)$ experienced by a Mn dopant ion inside a CdS/ZnS QD (Figure 5). The core/shell QD with a stoichiometric formula of $\text{Cd}_{288}\text{S}_{288}/\text{Zn}_{248}\text{S}_{248}$, having a core radius of 1.5 nm and a core/shell radius of 3.0 nm, was constructed from the bulk crystal structures. Using radial configuration integral $Z(r, T)$, we define the change in the radial Helmholtz free energy $\Delta A(r)$ as

$$\Delta A_{\text{eff}}(r) = A(r) - A(r_0) = -RT \ln \left[\frac{Z(r, T)}{Z(r_0, T)} \right] \quad (4)$$

where r_0 is the reference point. The free energy barrier associated with the migration/ejection of the dopant was used to calculate the rate constant of the movement $k(T)$ using transition-state theory:

$$k(T) = \frac{k_B T}{h} e^{-\Delta A^\ddagger / k_B T} \quad (5)$$

where ΔA^\ddagger is the free energy barrier along the transition path and h is Planck’s constant.

The calculated radial free energy for Mn dopants in CdS/ZnS QDs exhibits a local minimum at the core/shell interface of -0.111 eV at 300 °C [$r = 1.5$ nm (Figure S14)]. Therefore, the migration of the dopant from the core toward the core/shell interface can decrease the overall free energy after overcoming a small energy barrier within the CdS core ($\sim 4.25 \times 10^{-3}$ eV at $r = 0.8$ nm and 300 °C). However, a much higher energy barrier with a height of 1.59×10^{-2} eV presents in the ZnS shell region ($r = 1.5$ –3 nm at 300 °C) for the dopant ejection to solvent minimum. The higher and broader barrier for dopant ejection than for dopant migration to the core/shell

interface is consistent with the higher temperature required for dopant ejection than migration observed in our experiments. The rate constant of for the migration of the dopant to the core/shell interface was also found to be higher than that of dopant ejection (Figure 5b), demonstrating that the core/shell interface has a positive impact of increasing the rate of migration of the dopant from the core region.

In summary, we have studied the mass transport of both dopants and the host lattice in Mn:CdS/ZnS core/shell QDs. It was found that the dopant movement and location inside Mn:CdS/ZnS QDs are highly dependent upon the microcomposition of the host lattice and temperature. Three distinct stages of mass transport can be resolved, including (I) surface dopant replacement during the initial ZnS passivation, (II) migration of the dopant toward the alloyed interface of CdS/ZnS core/shell QDs weakening H–D coupling at $T < T_b$, and (III) global alloying of host QDs and dopant ejection restrengthening H–D coupling at $T > T_b$. The temperature- and lattice microcomposition-dependent dopant behaviors provide new ways to fine-tune the arrangement of the dopant inside QDs and consequently the H–D coupling-dependent properties of doped QDs.

■ ASSOCIATED CONTENT

SI Supporting Information

The Supporting Information is available free of charge at <https://pubs.acs.org/doi/10.1021/acs.jpcllett.0c01861>.

All synthetic methods, characterization data (XRD, transmission electron microscopy, XAFS, and EPR), optical data of the control experiments of Mn:CdS QDs and undoped CdS/ZnS core/shell QDs, DFT calculation, and thermal annealing data (optical and EPR) of Mn:CdS/ZnS core/shell QDs (PDF)

■ AUTHOR INFORMATION

Corresponding Authors

Arindam Chakraborty – Department of Chemistry, Syracuse University, Syracuse, New York 13244, United States; orcid.org/0000-0003-2710-0637; Email: archakra@syr.edu

Robert W. Meulenberg – Department of Physics and Astronomy and Frontier Institute for Research in Sensor Technologies, University of Maine, Orono, Maine 04469, United States; Email: robert.meulenberg@maine.edu

Weiwei Zheng – Department of Chemistry, Syracuse University, Syracuse, New York 13244, United States; orcid.org/0000-0003-1394-1806; Email: wzhen104@syr.edu

Authors

Elan Hofman – Department of Chemistry, Syracuse University, Syracuse, New York 13244, United States

Alex Khammang – Department of Physics and Astronomy and Frontier Institute for Research in Sensor Technologies, University of Maine, Orono, Maine 04469, United States

Joshua T. Wright – Department of Physics, Illinois Institute of Technology, Chicago, Illinois 60616, United States

Zhi-Jun Li – Department of Chemistry, Syracuse University, Syracuse, New York 13244, United States

Peter Francis McLaughlin – Department of Chemistry, Syracuse University, Syracuse, New York 13244, United States

Andrew Hunter Davis – Department of Chemistry, Syracuse University, Syracuse, New York 13244, United States

John Mark Franck – Department of Chemistry, Syracuse University, Syracuse, New York 13244, United States

Complete contact information is available at: <https://pubs.acs.org/doi/10.1021/acs.jpcllett.0c01861>

Notes

The authors declare no competing financial interest.

■ ACKNOWLEDGMENTS

W.Z. acknowledges support from a start-up grant from Syracuse University, ACS-PRF #59861-DNIS, and NSF CHE-1944978. Transmission electron microscopy measurements were performed at the Cornell Center for Materials Research (CCMR), which are supported through the NSF MRSEC program (DMR-1719875). The authors appreciate Dr. Boris Dzikovski for the assistance with EPR measurements. This work for ACERT was supported by National Institutes of Health Grant NIH/NIBIB R01EB00315. The work at the University of Maine and Illinois Institute of Technology was supported by National Science Foundation Grant DMR-1708617. Materials Research Collaborative Access Team (MRCAT) operations are supported by the U.S. Department of Energy (DOE) and the MRCAT member institutions. Portions of this research used resources of the Advanced Photon Source, a DOE Office of Science User Facility operated for the DOE Office of Science by Argonne National Laboratory under Contract DE-AC02-06CH11357. A. C. acknowledges support from NSF under Grant No. CHE-1349892.

■ REFERENCES

- (1) Norris, D. J.; Efros, A. L.; Erwin, S. C. Doped nanocrystals. *Science* **2008**, *319*, 1776–1779.
- (2) Erwin, S. C.; Zu, L. J.; Hafel, M. I.; Efros, A. L.; Kennedy, T. A.; Norris, D. J. Doping semiconductor nanocrystals. *Nature* **2005**, *436*, 91–94.
- (3) Mocatta, D.; Cohen, G.; Schattner, J.; Millo, O.; Rabani, E.; Banin, U. Heavily Doped Semiconductor Nanocrystal Quantum Dots. *Science* **2011**, *332*, 77–81.
- (4) Yu, J. H.; Liu, X.; Kweon, K. E.; Joo, J.; Park, J.; Ko, K. T.; Lee, D. W.; Shen, S.; Tivakornsasithorn, K.; Son, J. S.; Park, J. H.; Kim, Y. W.; Hwang, G. S.; Dobrowolska, M.; Furdyna, J. K.; Hyeon, T. Giant Zeeman splitting in nucleation-controlled doped CdSe:Mn²⁺ quantum nanoribbons. *Nat. Mater.* **2010**, *9*, 47–53.
- (5) Bryan, J. D.; Gamelin, D. R. Doped Semiconductor Nanocrystals: Synthesis, Characterization, Physical Properties, and Applications. *Prog. Inorg. Chem.* **2005**, *54*, 47–126.
- (6) Beaulac, R.; Schneider, L.; Archer, P. I.; Bacher, G.; Gamelin, D. R. Light-Induced Spontaneous Magnetization in Doped Colloidal Quantum Dots. *Science* **2009**, *325*, 973–976.
- (7) Zheng, W.; Strouse, G. F. Involvement of Carriers in the Size-Dependent Magnetic Exchange for Mn:CdSe Quantum Dots. *J. Am. Chem. Soc.* **2011**, *133*, 7482–7489.
- (8) Zheng, W.; Kumar, P.; Washington, A.; Wang, Z.; Dalal, N. S.; Strouse, G. F.; Singh, K. Quantum Phase Transition from Superparamagnetic to Quantum Superparamagnetic State in Ultrasmall Cd_{1-x}Cr(II)_xSe Quantum Dots? *J. Am. Chem. Soc.* **2012**, *134*, 2172–2179.
- (9) Zandi, O.; Agrawal, A.; Shearer, A. B.; Reimnitz, L. C.; Dahlman, C. J.; Staller, C. M.; Milliron, D. J. Impacts of surface depletion on the plasmonic properties of doped semiconductor nanocrystals. *Nat. Mater.* **2018**, *17*, 710–717.
- (10) Pradhan, N.; Das Adhikari, S.; Nag, A.; Sarma, D. D. Luminescence, Plasmonic, and Magnetic Properties of Doped

- Semiconductor Nanocrystals. *Angew. Chem., Int. Ed.* **2017**, *56*, 7038–7054.
- (11) Knowles, K. E.; Hartstein, K. H.; Kilburn, T. B.; Marchioro, A.; Nelson, H. D.; Whitham, P. J.; Gamelin, D. R. Luminescent Colloidal Semiconductor Nanocrystals Containing Copper: Synthesis, Photo-physics, and Applications. *Chem. Rev.* **2016**, *116*, 10820–10851.
- (12) McLaurin, E. J.; Vlaskin, V. A.; Gamelin, D. R. Water-Soluble Dual-Emitting Nanocrystals for Ratiometric Optical Thermometry. *J. Am. Chem. Soc.* **2011**, *133*, 14978–14980.
- (13) Beaulac, R.; Archer, P. I.; Ochsenbein, S. T.; Gamelin, D. R. Mn²⁺-Doped CdSe Quantum Dots: New Inorganic Materials for Spin-Electronics and Spin-Photonics. *Adv. Funct. Mater.* **2008**, *18*, 3873–3891.
- (14) Santra, P. K.; Kamat, P. V. Mn-Doped Quantum Dot Sensitized Solar Cells: A Strategy to Boost Efficiency over 5%. *J. Am. Chem. Soc.* **2012**, *134*, 2508–2511.
- (15) Li, Z.; Xiao, C.; Zhu, H.; Xie, Y. Defect Chemistry for Thermoelectric Materials. *J. Am. Chem. Soc.* **2016**, *138*, 14810–14819.
- (16) Wu, P.; Yan, X.-P. Doped quantum dots for chemo/biosensing and bioimaging. *Chem. Soc. Rev.* **2013**, *42*, 5489–5521.
- (17) Yang, Y.; Chen, O.; Angerhofer, A.; Cao, Y. C. On Doping CdS/ZnS Core/Shell Nanocrystals with Mn. *J. Am. Chem. Soc.* **2008**, *130*, 15649–15661.
- (18) Yang, Y.; Chen, O.; Angerhofer, A.; Cao, Y. C. Radial-Position-Controlled Doping in CdS/ZnS Core/Shell Nanocrystals. *J. Am. Chem. Soc.* **2006**, *128*, 12428–12429.
- (19) Hofman, E.; Robinson, R. J.; Li, Z.-J.; Dzikovski, B.; Zheng, W. Controlled Dopant Migration in CdS/ZnS Core/Shell Quantum Dots. *J. Am. Chem. Soc.* **2017**, *139*, 8878–8885.
- (20) Lounis, S. D.; Runnerstrom, E. L.; Bergerud, A.; Nordlund, D.; Milliron, D. J. Influence of Dopant Distribution on the Plasmonic Properties of Indium Tin Oxide Nanocrystals. *J. Am. Chem. Soc.* **2014**, *136*, 7110–7116.
- (21) Staller, C. M.; Robinson, Z. L.; Agrawal, A.; Gibbs, S. L.; Greenberg, B. L.; Lounis, S. D.; Kortshagen, U. R.; Milliron, D. J. Tuning Nanocrystal Surface Depletion by Controlling Dopant Distribution as a Route Toward Enhanced Film Conductivity. *Nano Lett.* **2018**, *18*, 2870–2878.
- (22) Lee, W.; Oh, J.; Kwon, W.; Lee, S. H.; Kim, D.; Kim, S. Synthesis of Ag/Mn Co-Doped CdS/ZnS (Core/Shell) Nanocrystals with Controlled Dopant Concentration and Spatial Distribution and the Dynamics of Excitons and Energy Transfer between Co-Dopants. *Nano Lett.* **2019**, *19*, 308–317.
- (23) Zheng, W.; Singh, K.; Wang, Z.; Wright, J. T.; van Tol, J.; Dalal, N. S.; Meulenberg, R. W.; Strouse, G. F. Evidence of a ZnCr₂Se₄ Spinel Inclusion at the Core of a Cr-Doped ZnSe Quantum Dot. *J. Am. Chem. Soc.* **2012**, *134*, 5577–5585.
- (24) Pradhan, N.; Goorskey, D.; Thessing, J.; Peng, X. An Alternative of CdSe Nanocrystal Emitters: Pure and Tunable Impurity Emissions in ZnSe Nanocrystals. *J. Am. Chem. Soc.* **2005**, *127*, 17586–17587.
- (25) Pradhan, N.; Peng, X. Efficient and Color-Tunable Mn-Doped ZnSe Nanocrystal Emitters: Control of Optical Performance via Greener Synthetic Chemistry. *J. Am. Chem. Soc.* **2007**, *129*, 3339–3347.
- (26) Viswanatha, R.; Brovelli, S.; Pandey, A.; Crooker, S. A.; Klimov, V. I. Copper-Doped Inverted Core/Shell Nanocrystals with “Permanent” Optically Active Holes. *Nano Lett.* **2011**, *11*, 4753–4758.
- (27) Mikulec, F. V.; Kuno, M.; Bennati, M.; Hall, D. A.; Griffin, R. G.; Bawendi, M. G. Organometallic Synthesis and Spectroscopic Characterization of Manganese-Doped CdSe Nanocrystals. *J. Am. Chem. Soc.* **2000**, *122*, 2532–2540.
- (28) Kato, F.; Kittilstved, K. R. Site-Specific Doping of Mn²⁺ in a CdS-Based Molecular Cluster. *Chem. Mater.* **2018**, *30*, 4720–4727.
- (29) Vlaskin, V. A.; Barrows, C. J.; Erickson, C. S.; Gamelin, D. R. Nanocrystal Diffusion Doping. *J. Am. Chem. Soc.* **2013**, *135*, 14380–14389.
- (30) Barrows, C. J.; Chakraborty, P.; Kornowske, L. M.; Gamelin, D. R. Tuning Equilibrium Compositions in Colloidal Cd_{1-x}Mn_xSe Nanocrystals Using Diffusion Doping and Cation Exchange. *ACS Nano* **2016**, *10*, 910–918.
- (31) Buonsanti, R.; Milliron, D. J. Chemistry of Doped Colloidal Nanocrystals. *Chem. Mater.* **2013**, *25*, 1305–1317.
- (32) Chen, D.; Viswanatha, R.; Ong, G. L.; Xie, R.; Balasubramanian, M.; Peng, X. Temperature Dependence of “Elementary Processes” in Doping Semiconductor Nanocrystals. *J. Am. Chem. Soc.* **2009**, *131*, 9333–9339.
- (33) Zu, L. J.; Norris, D. J.; Kennedy, T. A.; Erwin, S. C.; Efros, A. L. Impact of ripening on manganese-doped ZnSe nanocrystals. *Nano Lett.* **2006**, *6*, 334–340.
- (34) Dalpian, G. M.; Chelikowsky, J. R. Self-Purification in Semiconductor Nanocrystals. *Phys. Rev. Lett.* **2006**, *96*, 226802.
- (35) Li, Z.-J.; Hofman, E.; Blaker, A.; Davis, A. H.; Dzikovski, B.; Ma, D.-K.; Zheng, W. Interface Engineering of Mn-Doped ZnSe-Based Core/Shell Nanowires for Tunable Host–Dopant Coupling. *ACS Nano* **2017**, *11*, 12591–12600.
- (36) Chen, D.; Zhao, F.; Qi, H.; Rutherford, M.; Peng, X. Bright and Stable Purple/Blue Emitting CdS/ZnS Core/Shell Nanocrystals Grown by Thermal Cycling Using a Single-Source Precursor. *Chem. Mater.* **2010**, *22*, 1437–1444.
- (37) Nag, A.; Chakraborty, S.; Sarma, D. D. To Dope Mn²⁺ in a Semiconducting Nanocrystal. *J. Am. Chem. Soc.* **2008**, *130*, 10605–10611.
- (38) Zheng, W.; Wang, Z.; Wright, J.; Goundie, B.; Dalal, N. S.; Meulenberg, R. W.; Strouse, G. F. Probing the Local Site Environments in Mn:CdSe Quantum Dots. *J. Phys. Chem. C* **2011**, *115*, 23305–23314.
- (39) Zheng, W.; Wang, Z.; van Tol, J.; Dalal, N. S.; Strouse, G. F. Alloy Formation at the Tetrapod Core/Arm Interface. *Nano Lett.* **2012**, *12*, 3132–3137.
- (40) Yang, Y.; Chen, O.; Angerhofer, A.; Cao, Y. C. Radial-position-controlled doping of CdS/ZnS core/shell nanocrystals: surface effects and position-dependent properties. *Chem. - Eur. J.* **2009**, *15*, 3186–3197.
- (41) Shannon, R. Revised effective ionic radii and systematic studies of interatomic distances in halides and chalcogenides. *Acta Crystallogr., Sect. A: Cryst. Phys., Diffr., Theor. Gen. Crystallogr.* **1976**, *32*, 751–767.
- (42) Zu, L.; Norris, D. J.; Kennedy, T. A.; Erwin, S. C.; Efros, A. L. Impact of Ripening on Manganese-Doped ZnSe Nanocrystals. *Nano Lett.* **2006**, *6*, 334–340.
- (43) Chen, H.-Y.; Maiti, S.; Son, D. H. Doping Location-Dependent Energy Transfer Dynamics in Mn-Doped CdS/ZnS Nanocrystals. *ACS Nano* **2012**, *6*, 583–591.
- (44) Ithurria, S.; Guyot-Sionnest, P.; Mahler, B.; Dubertret, B. Mn²⁺ as a radial pressure gauge in colloidal core/shell nanocrystals. *Phys. Rev. Lett.* **2007**, *99*, 265501.
- (45) Wang, Z.; Meijerink, A. Concentration Quenching in Upconversion Nanocrystals. *J. Phys. Chem. C* **2018**, *122*, 26298–26306.
- (46) Li, Z.-J.; Hofman, E.; Davis, A. H.; Khamrang, A.; Wright, J. T.; Dzikovski, B.; Meulenberg, R. W.; Zheng, W. Complete Dopant Substitution by Spinodal Decomposition in Mn-Doped Two-Dimensional CsPbCl₃ Nanoplatelets. *Chem. Mater.* **2018**, *30*, 6400–6409.
- (47) Chakraborty, P.; Jin, Y.; Barrows, C. J.; Dunham, S. T.; Gamelin, D. R. Kinetics of Isovalent (Cd²⁺) and Aliovalent (In³⁺) Cation Exchange in Cd_{1-x}Mn_xSe Nanocrystals. *J. Am. Chem. Soc.* **2016**, *138*, 12885–12893.